

HCO mapping of the Horsehead : Tracing the illuminated dense molecular cloud surfaces^{*}

Maryvonne Gerin¹, Javier R. Goicoechea^{1**}, Jerome Pety^{2,1}, and Pierre Hily-Blant³

¹ LERMA–LRA, UMR 8112, CNRS, Observatoire de Paris and Ecole Normale Supérieure, 24 Rue Lhomond, 75231 Paris, France.
e-mail: maryvonne.gerin@lra.ens.fr, jrgoicoechea@fis.ucm.es

² IRAM, 300 rue de la Piscine, 38406 Grenoble cedex, France.
e-mail: pety@iram.fr

³ Laboratoire d’Astrophysique, Observatoire de Grenoble, BP 53, 38041 Grenoble Cedex 09, France.
e-mail: pierre.hilyblant@obs.ujf-grenoble.fr

Received September 2008 ; accepted xxx 2008

ABSTRACT

Context. Far-UV photons strongly affect the physical and chemical state of molecular gas in the vicinity of young massive stars.

Aims. Finding molecular tracers of the presence of FUV radiation fields in the millimeter wavelength domain is desirable, because IR diagnostics (PAHs for instance) are not easily accessible towards high extinction line-of-sights. Furthermore, gas phase diagnostics provide information on the velocity fields.

Methods. We have obtained maps of the HCO and H¹³CO⁺ ground state lines towards the Horsehead edge at 5'' angular resolution with a combination of Plateau de Bure Interferometer (PdBI) and the IRAM-30m telescope observations. These maps have been complemented with IRAM-30m observations of several excited transitions at two different positions.

Results. Bright formyl radical emission delineates the illuminated edge of the nebula, with a faint emission remaining towards the shielded molecular core. Viewed from the illuminated star, the HCO emission almost coincides with the PAH and CCH emission. HCO reaches a similar abundance than HCO⁺ in the PDR ($\approx 1-2 \times 10^{-9}$ with respect to H₂). To our knowledge, this is the highest HCO abundance ever measured. Pure gas-phase chemistry models fail to reproduce the observed HCO abundance by ~ 2 orders of magnitude, except if reactions of atomic oxygen with carbon radicals abundant in the PDR (i.e., CH₂) play a significant role in the HCO formation. Alternatively, HCO could be produced in the PDR by non-thermal processes such as photo-processing of ice mantles and subsequent photo-desorption of either HCO or H₂CO, and further gas phase photodissociation.

Conclusions. The measured HCO/H¹³CO⁺ abundance ratio is large towards the PDR (≈ 50), and much lower toward the gas shielded from FUV radiation (≤ 1). We propose that high HCO abundances ($\geq 10^{-10}$) together with large HCO/H¹³CO⁺ abundance ratios (≥ 1) are sensitive diagnostics of the presence of active photochemistry induced by FUV radiation.

Key words. Astrochemistry – ISM clouds – molecules – individual object (Horsehead nebula) – radiative transfer – radio lines: ISM

1. Introduction

Photodissociation region (PDR) models are used to understand the evolution of far-UV (FUV; $h\nu < 13.6$ eV) illuminated matter both in our Galaxy and in external galaxies. These sophisticated models have been benchmarked recently (Röllig et al. 2007) and are continuously upgraded (e.g., Goicoechea & Le Bourlot 2007; González-García et al. 2008). Given the large number of physical and chemical processes included in such models, it is necessary to build reference data sets, which can be used to test the predictive accuracy of models. Our team has contributed to this goal by providing a series of high resolution interferometric observations of the Horsehead nebula (see Pety et al. 2007b, for a summary). Indeed, this source is particularly well suited because of its favorable orientation and geometry, and its moderate distance (~ 400 pc; Habart et al. 2005). We have previously studied the carbon (Teyssier et al. 2004;

Pety et al. 2005) and sulfur chemistry (Goicoechea et al. 2006), and detected the presence of a cold dense core, with active deuterium fractionation (Pety et al. 2007a).

The formyl radical, HCO, is known to be present in the interstellar medium since the late 70’s (Snyder et al. 1976). Snyder et al. (1985) give a detailed description of the HCO structure and discuss the energy diagram for the lowest energy levels. HCO is a bent triatomic asymmetric top with an unpaired electron. *a*-type and *b*-type transitions are allowed, with a stronger dipole moment (1.36 Debye) for the *a*-type transitions (Landsberg et al. 1977), which are therefore more easily detectable. The strongest HCO ground state transitions lie at 86.670, 86.708, 86.777 and 86.805 GHz, very close to the ground state transition of H¹³CO⁺ and to the first rotationally excited SiO line. Therefore HCO can be observed simultaneously with SiO and H¹³CO⁺. HCO ground state lines have been detected in the Orion Bar as well as in the dense PDRs NGC 2023, NGC 7023 and S 140 (Schilke et al. 2001). From limited mapping, they have shown that HCO is sharply peaked in the Orion Bar PDR, confirming earlier suggestions that HCO is a tracer of the cloud illuminated interfaces (de Jong et al. 1980). García-Burillo et al. (2002) have mapped HCO and H¹³CO⁺ in the nearby galaxy M82. HCO, CO and the ionized gas present a

Send offprint requests to: e-mail: maryvonne.gerin@lra.ens.fr

^{*} Based on observations obtained with the IRAM Plateau de Bure interferometer and 30 m telescope. IRAM is supported by INSU/CNRS (France), MPG (Germany), and IGN (Spain).

^{**} Current address: Departamento de Astrofísica. Universidad Complutense de Madrid, Spain.

Table 1. Observation parameters for the maps shown in Fig. 1 and 5 (Fig. 5 is available on-line only). The projection center of all the maps is $\alpha_{2000} = 05^h40^m54.27^s$, $\delta_{2000} = -02^{\circ}28'00''$.

Molecule	Transition	Frequency GHz	Instrument	Config.	Beam arcsec	PA °	Vel. Resol. km s ⁻¹	Int. Time ^a hours	T _{sys} K	Noise ^b K	Obs. date
H ¹³ CO ⁺	1 – 0	86.754288	PdBI	C & D	6.76 × 4.65	13	0.2	6.5	150	0.10	2006-2007
HCO	1 _{0,1} 3/2, 2 – 0 _{0,0} 1/2, 1	86.670760	PdBI	C & D	6.69 × 4.39	16	0.2	6.5	150	0.09	2006-2007
CCH	1, 3/2(2) – 0, 1/2(1)	87.316925	PdBI	C & D	7.24 × 4.99	54	0.2	6.9	130	0.07	2002-2003

^a On-source time computed as if the source were always observed with 6 antennae. ^b The noise values quoted here are the noises at the mosaic phase center (Mosaic noise is inhomogeneous due to primary beam correction; it steeply increases at the mosaic edges).

Molecule	Transition	Frequency GHz	Instrument	# Pix.	F _{eff}	B _{eff}	Resol. arcsec	Resol. km s ⁻¹	Int. Time ^a hours	T _{sys} K	Noise mK	Obs. date
H ¹³ CO ⁺	J=1–0	86.754288	30m/AB100	2	0.95	0.78	28.4	0.2	2.6/5.0	133	69	2006-2007
HCO	1 _{0,1} 3/2, 2 – 0 _{0,0} 1/2, 1	86.670760	30m/AB100	2	0.95	0.78	29.9	0.2	2.6/5.0	133	63	2006-2007
HCO	1 _{0,1} 3/2, 1 – 0 _{0,0} 1/2, 0	86.708360	30m/AB100	2	0.95	0.78	29.9	0.2	2.6/5.0	133	63	2006-2007
HCO	1 _{0,1} 1/2, 1 – 0 _{0,0} 1/2, 1	86.777460	30m/AB100	2	0.95	0.78	29.9	0.2	2.6/5.0	133	66	2006-2007
HCO	1 _{0,1} 1/2, 0 – 0 _{0,0} 1/2, 1	86.805780	30m/AB100	2	0.95	0.78	29.9	0.2	2.6/5.0	133	66	2006-2007

^a Two values are given for the integration time: the on-source time and the telescope time.

Table 2. Observation parameters for the HCO deep integrations shown in Fig. 1. Associated transitions can be found in Table 3. The RA and Dec offsets are computed with reference to $\alpha_{2000} = 05^h40^m54.27^s$, $\delta_{2000} = -02^{\circ}28'00''$. The positions are also given in the coordinate system used to display the maps in Fig. 1 and 5. In this coordinate system, maps are rotated by 14° counter-clockwise around the projection center, located at $(\delta x, \delta y) = (20'', 0'')$, to bring the illuminated star direction in the horizontal direction and the horizontal zero has been set at the PDR edge.

Position name	(δ RA, δ Dec) arcsec	($\delta x, \delta y$) arcsec
“DCO ⁺ peak”	(20'', 22'')	(44.7'', 16.5'')
“HCO peak”	(–5, 0'')	(15.1'', 1.2'')

Position	Frequency GHz	Line area ^a K km s ⁻¹	Instrument	F _{eff}	B _{eff}	Resol. arcsec	Resol. km s ⁻¹	Int. Time ^b hours	T _{sys} K	Noise mK	Obs. date
“DCO ⁺ peak”	86.670760	0.23 ± 0.009	30m/B100	0.95	0.78	28.4	0.27	0.75/1.5	134	11	2008
	86.708360	0.12 ± 0.009	30m/B100	0.95	0.78	28.4	0.27	0.75/1.5	134	11	2008
“HCO peak”	86.670760	0.52 ± 0.008	30m/B100	0.95	0.78	28.4	0.27	0.75/1.5	127	10	2008
	86.708360	0.31 ± 0.007	30m/B100	0.95	0.78	28.4	0.27	0.75/1.5	127	10	2008
	173.3773770	0.47 ± 0.023	30m/C150	0.93	0.65	14.2	0.067	2.0/4.0	667	66	2008
	173.4060816	0.26 ± 0.018	30m/C150	0.93	0.65	14.2	0.067	2.0/4.0	667	66	2008
	173.4430648	0.23 ± 0.020	30m/C150	0.93	0.65	14.2	0.067	2.0/4.0	667	66	2008
	260.0603290	0.16 ± 0.019	30m/C270	0.88	0.46	9.5	0.18	3.0/6.0	740	59	2008
	260.0821920	0.14 ± 0.020	30m/C270	0.88	0.46	9.5	0.18	3.0/6.0	740	59	2008
	260.1335860	0.12 ± 0.017	30m/C270	0.88	0.46	9.5	0.18	3.0/6.0	740	59	2008
260.1557690	0.06 ± 0.016	30m/C270	0.88	0.46	9.5	0.18	3.0/6.0	740	59	2008	

^a Values obtained from Gaussian fits performed on the spectra using the main beam temperature scale. ^b Two values are given for the integration time: the on-source time and the telescope time.

nested ring morphology, with the HCO peaks being located further out compared to CO and the ring of H II regions. The chemistry of HCO is not well understood. Schilke et al. (2001) concluded that it is extremely difficult to understand the observed HCO abundance in PDRs with gas phase chemistry alone. As a possible way out, they tested the production of HCO by the photodissociation of formaldehyde. In this model, H₂CO is produced in grain mantles, and released by non-thermal photodesorption in the gas phase in the PDR. However, even with this favorable hypothesis, the model can not reproduce the abundance and spatial distribution of HCO because the photoproduction is most efficient at an optical depth of a few magnitudes where the photodissociation becomes less effective.

In this paper, we present maps of the formyl radical ground state lines at high angular resolution towards the Horsehead neb-

ula, and the detection of higher energy level transitions towards two particular lines of sights, one in the PDR region and the other in the associated dense core. These observations enable us to accurately study the HCO spatial distribution and abundance. We present the observations and data reduction in section 2, while the results and HCO abundance are given in section 3, and the discussion of HCO chemistry and PDR modeling is given in section 4.

2. Observations and data reduction

Tables 1 and 2 summarize the observation parameters for the data obtained with the IRAM PdBI and 30m telescopes. The HCO ground state lines were observed simultaneously with H¹³CO⁺ and SiO. Frequency-switched, on-the-fly maps of the

H^{13}CO^+ $J=1-0$ and HCO ground state lines (see Fig. 5), obtained at the IRAM-30m using the A100 and B100 3mm receivers (~ 7 mm of water vapor) were used to produce the short-spacings needed to complement a 7-field mosaic acquired with the 6 PdBI antennae in the CD configuration (baseline lengths from 24 to 176 m). The whole PdBI data set will be comprehensively described in a forthcoming paper studying the fractional ionization across the Horsehead edge (Goicoechea et al. 2009, in prep.). The CCH data shown in Fig. 1 have been extensively described in Pety et al. 2005. The high resolution HCO $1_{0,1} - 0_{0,0}$ data are complemented by observations of the $2_{0,2} - 1_{0,1}$ and $3_{0,3} - 2_{0,2}$ multiplets with the IRAM 30m telescope centered on the PDR and the dense core. To obtain those deep integration spectra, we used the position switching observing mode. The on-off cycle duration was 1 minute and the off-position offsets were $(\delta RA, \delta Dec) = (-100'', 0'')$, *i.e.* the H II region ionized by σ Ori and free of molecular emission. Position accuracy is estimated to be about $3''$ for the 30m data and less than $0.5''$ for the PdBI data.

The data processing was done with the GILDAS¹ softwares (Pety 2005b). The IRAM-30m data were first calibrated to the T_A^* scale using the chopper wheel method (Penzias & Burrus 1973), and finally converted to main beam temperatures (T_{mb}) using the forward and main beam efficiencies (F_{eff} & B_{eff}) displayed in Table 2. The resulting amplitude accuracy is $\sim 10\%$. Frequency-switched spectra were folded using the standard shift-and-add method, after baseline subtraction. The resulting spectra were finally gridded through convolution by a Gaussian. Position-switched spectra were co-added before baseline subtraction. Interferometric data and short-spacing data were merged before imaging and deconvolution of the mosaic, using standard techniques of GILDAS (see *e.g.* Pety et al. 2005, for details).

3. Results and Discussion

3.1. Spatial distribution

Fig. 1 shows a map of the integrated intensity of the strongest HCO line at 86.671 GHz, of the H^{13}CO^+ $J=1-0$ line and of the strongest CCH line at 87.317 GHz. Fig. 2 displays high signal-to-noise ratio spectra of several hyperfine components of three HCO rotational transitions towards the HCO and the DCO^+ emission peaks.

Most of the formyl radical emission is concentrated in a narrow structure, delineating the edge of the Horsehead nebula. Low level emission is however detected throughout the nebula, including towards the dense core identified by its strong DCO^+ and H^{13}CO^+ emission (Pety et al. 2007a). The HCO emission is resolved by our PdBI observations. From 2-dimensional Gaussian fits of the image, we estimate that the emission width is $\sim 13 \pm 4''$ in the plane of the sky. The H^{13}CO^+ emission shows a different pattern : most of the signal is associated with the dense core behind the photodissociation front, and faint H^{13}CO^+ emission detected in the illuminated edge. The CCH emission pattern is less extreme than HCO, but shows a similar enhancement in the PDR.

In summary, the morphology of the HCO emission is reminiscent of the emission of the PDR tracers, either the PAH emission (Abergel et al. 2002) or the small hydrocarbons emission, which is strongly enhanced towards the

Table 3. Einstein coefficients and upper level energies.

Molecule	Transition $J, F - J', F'$	Frequency GHz	A_{ij} (s^{-1})	E_{up} (K)
HCO	$1_{01} - 0_{00}$			
	$3/2, 2 - 1/2, 1$	86.670760	4.69×10^{-6}	4.2
	$3/2, 1 - 1/2, 0$	86.708360	4.60×10^{-6}	4.2
	$1/2, 1, 1/2, 0$	86.777460	4.61×10^{-6}	4.2
	$1/2, 0 - 1/2, 1$	86.805780	4.71×10^{-6}	4.2
	$2_{02} - 1_{01}$			
	$5/2, 3 - 3/2, 2$	173.3773770	4.51×10^{-5}	12.5
	$5/2, 2 - 3/2, 1$	173.4060816	4.43×10^{-5}	12.5
	$3/2, 2 - 1/2, 1$	173.4430648	3.39×10^{-5}	12.5
	$3_{03} - 2_{02}$			
	$7/2, 4 - 5/2, 3$	260.0603290	1.63×10^{-4}	25.0
	$7/2, 3 - 5/2, 2$	260.0821920	1.61×10^{-4}	25.0
	$5/2, 3 - 3/2, 2$	260.1335860	1.45×10^{-4}	25.0
$5/2, 2 - 3/2, 1$	260.1557690	1.37×10^{-4}	25.0	
H^{13}CO^+	$J=1-0$	86.754288	3.2×10^{-5}	4.2
	$J=3-2$	260.2553390	1.3×10^{-3}	25.0

The line frequencies and intensities were extracted from the JPL (Pickett et al. 1998) and CDMS (Müller et al. 2001; Müller et al. 2005) molecular spectroscopy data bases for HCO and H^{13}CO^+ respectively.

PDR (Teyssier et al. 2004; Pety et al. 2005). By contrast, the HCO emission becomes strikingly faint where the gas is dense and shielded from FUV radiation. These regions are associated with bright DCO^+ and H^{13}CO^+ emission (Pety et al. 2007a). Our maps therefore confirm that HCO is a PDR species.

3.2. Column densities and abundances

3.2.1. Radiative transfer models of HCO and H^{13}CO^+

Einstein coefficients and upper level energies of the studied HCO and H^{13}CO^+ lines are given in Table 3. As no collisional cross-sections with H_2 nor He have been calculated for HCO so far, we have computed the HCO column densities assuming a single excitation temperature T_{ex} for all transitions. Nevertheless our calculation takes into account thermal, turbulent and opacity broadening as well as the cosmic microwave background and line opacity (Goicoechea et al. 2006). For H^{13}CO^+ , detailed non-local and non-LTE excitation and radiative transfer calculations have been performed using the same approach as in our previous PdBI CS and C^{18}O line analysis (see Appendix in Goicoechea et al. 2006). H^{13}CO^+ - H_2 collisional rate coefficients were adapted from those of Flower (1999) for HCO^+ , and specific H^{13}CO^+ -electron rates were kindly provided by Faure & Tennyson (in prep.).

3.2.2. Structure of the PDR in HCO and H^{13}CO^+

To get more insight on the spatial variation of the HCO and H^{13}CO^+ column densities and abundances, we have analyzed a cut through the PDR, centered on the ‘‘HCO peak’’ at $\delta y=0''$ (see Fig. 3). The cut clearly shows that HCO is brighter than H^{13}CO^+ in the PDR and vice-versa in the dense core. Taking into account the different level degeneracies of both transitions (a factor 2.4) and the fact that the associated Einstein coefficients A_{ij} differ by a factor ~ 8 (due to the different permanent dipole moments, see Table 3), $N(\text{H}^{13}\text{CO}^+)$ must be significantly lower than $N(\text{HCO})$ towards the PDR.

¹ See <http://www.iram.fr/IRAMFR/GILDAS> for more information about the GILDAS softwares.

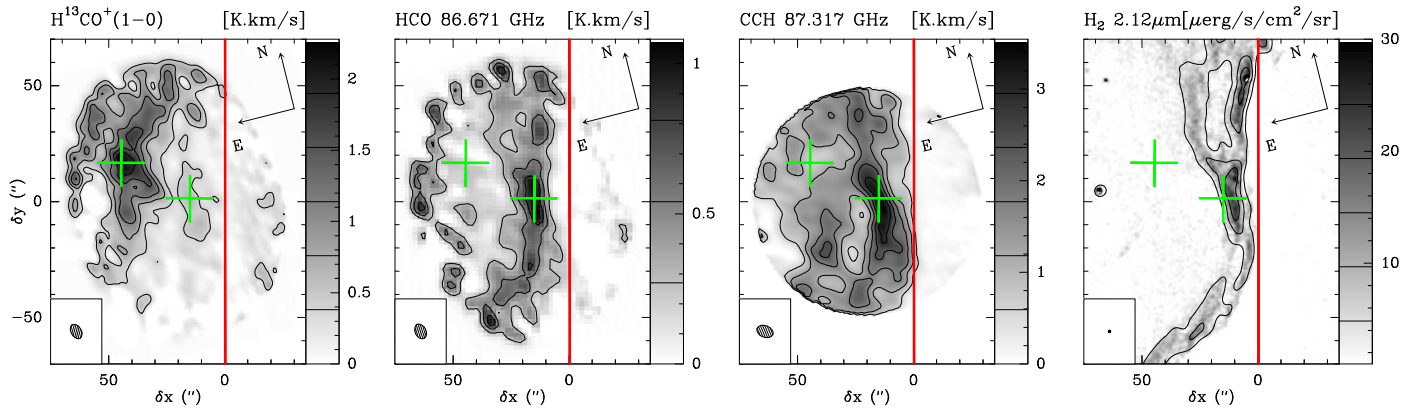


Fig. 1. High angular resolution maps of the integrated intensity of H^{13}CO^+ , HCO, CCH and vibrationally excited H_2 emission. H^{13}CO^+ and HCO have been observed simultaneously, both with the IRAM-30m and IRAM-PdBI. Maps have been rotated by 14° counter-clockwise around the projection center, located at $(\delta x, \delta y) = (20'', 0'')$, to bring the illuminated star direction in the horizontal direction and the horizontal zero has been set at the PDR edge. The emission of all lines is integrated between 10.1 and 11.1 km s^{-1} . Displayed integrated intensities are expressed in the main beam temperature scale. Contour levels are displayed on the grey scale lookup tables. The red vertical line shows the PDR edge and the green crosses show the positions (DCO⁺ and HCO peaks) where deep integrations have been performed at IRAM-30m (see Fig. 2). The H_2 map is taken from (author?) (Habart et al. 2005).

We modeled the PDR as an edge-on cloud inclined by $\sim 5^\circ$ relative to the line-of-sight. We have chosen a cloud depth of $\sim 0.1 \text{ pc}$, which implies an extinction of $A_V \approx 20 \text{ mag}$ for the considered densities towards the ‘‘HCO peak’’. These parameters are the best geometrical description of the Horsehead PDR-edge (e.g., Habart et al. 2005) and also reproduce the observed 1.2 mm continuum emission intensity. The details of this modeling will be presented in Goicoechea et al. (2009). In the following, we describe in details the determination of the column densities and abundances for two particular positions, namely the ‘‘HCO peak’’ and the ‘‘DCO⁺ peak’’ (offsets relative to the map center can be found in Table 2).

3.2.3. HCO column densities

We used the three detected rotational transitions of HCO (each with several hyperfine components, see Fig. 2) to estimate the HCO column densities in the direction of the ‘‘HCO’’ peak. We have taken into account the varying beam dilution factors of the HCO emission at the ‘‘HCO peak’’ by modeling the HCO emission as a Gaussian filament of $\sim 12''$ width in the δx direction, and infinite in the δy direction. The filling factors at 260, 173 and 87 GHz are thus $\sim 0.8, 0.6$ and 0.4 , respectively.

A satisfactory fit of the IRAM-30m data towards the ‘‘HCO peak’’ is obtained for $T_{\text{ex}} \approx 5 \text{ K}$ and a turbulent velocity dispersion of $\sigma = 0.225 \text{ km s}^{-1}$ (FWHM = $2.355 \times \sigma$). Line profiles are reproduced for $N(\text{HCO}) = 3.2 \times 10^{13} \text{ cm}^{-2}$ (see red solid curves in Fig. 2). The most intense HCO lines at 86.67 and 173.38 GHz become marginally optically thick at this column density ($\tau \gtrsim 1$). Therefore, opacity corrections need to be taken into account. We checked that the low value of T_{ex} (subthermal excitation as $T_k \approx 60 \text{ K}$) is consistent with detailed excitation calculations carried for H^{13}CO^+ in the PDR which are described below.

Because the HCO signals are weaker towards the ‘‘DCO⁺ peak’’, we only detected 2 hyperfine components of the $1_{01} - 0_{00}$ transition. Assuming extended emission and the same excitation temperature as for the ‘‘HCO peak’’, 5 K , we fit the observed lines with a column density of $4.6 \times 10^{12} \text{ cm}^{-2}$ (blue solid lines in Fig. 2). Both HCO lines are optically thin at this position. This simple analysis shows that the HCO column density

Table 4. Inferred column densities and abundances with respect to molecular hydrogen, e.g. $\chi(\text{X}) = N(\text{X})/N(\text{H}_2)$.

Molecule	Method	HCO peak	DCO ⁺ peak
$N(\text{H}_2) [\text{cm}^{-2}]$	1.2 mm cont.	1.9×10^{22}	2.9×10^{22}
$N(\text{HCO}) [\text{cm}^{-2}]$	$T_{\text{ex}} = 5 \text{ K}$	3.2×10^{13}	4.6×10^{12}
$N(\text{H}^{13}\text{CO}^+) [\text{cm}^{-2}]$	Full excitation	5.8×10^{11}	$5.0 \times 10^{12} *$
$N(\text{HCO}^+) [\text{cm}^{-2}]$	$^{12}\text{C}/^{13}\text{C} = 60$	3.5×10^{13}	3.0×10^{14}
$\chi(\text{HCO})$		1.7×10^{-9}	$1.6 \times 10^{-10} \dagger$
$\chi(\text{H}^{13}\text{CO}^+)$		3.1×10^{-11}	1.7×10^{-10}
$\chi(\text{HCO}^+)$		1.8×10^{-9}	1.0×10^{-8}

* Pety et al. (2007a) $\dagger 1.7 \times 10^{-9}$ if HCO arises only from the cloud surface ($A_V \approx 3$).

is ~ 7 times larger at the ‘‘HCO peak’’ in the PDR, than towards the dense cold core.

3.2.4. H^{13}CO^+ column densities

Both the H^{13}CO^+ $J=3-2$ and $1-0$ line profiles at the ‘‘HCO peak’’ are fitted with $n(\text{H}_2) \approx 5 \times 10^4 \text{ cm}^{-3}$, $T_k \approx 60 \text{ K}$ and $e^-/\text{H} \approx 5 \times 10^{-5}$ (as predicted by the PDR models below). The required column density is $N(\text{H}^{13}\text{CO}^+) = 5.8 \times 10^{11} \text{ cm}^{-2}$. For those conditions, the excitation temperature, T_{ex} , of the $J=3-2$ transition varies from ≈ 4 to 6 K , which supports the single- T_{ex} models of HCO. Both H^{13}CO^+ lines are optically thin towards the ‘‘HCO peak’’.

The H^{13}CO^+ line emission towards the ‘‘DCO⁺ peak’’ has been studied by Pety et al. (2007a). Both H^{13}CO^+ lines are moderately optically thick towards the core, and the H^{13}CO^+ column density is $N(\text{H}^{13}\text{CO}^+) \approx 5.0 \times 10^{12} \text{ cm}^{-2}$, which represents an enhancement of nearly one order of magnitude relative to the PDR. According to our 1.2 mm continuum map, the extinction towards the core is $A_V \gtrsim 30 \text{ mag}$ compared to 20 mag in the PDR. The H^{13}CO^+ column density enhancement therefore corresponds to a true abundance enhancement.

3.2.5. Comparison of HCO and H^{13}CO^+ abundances

Table 4 summarizes the inferred HCO and H^{13}CO^+ column densities and abundances towards the 2 selected positions : the

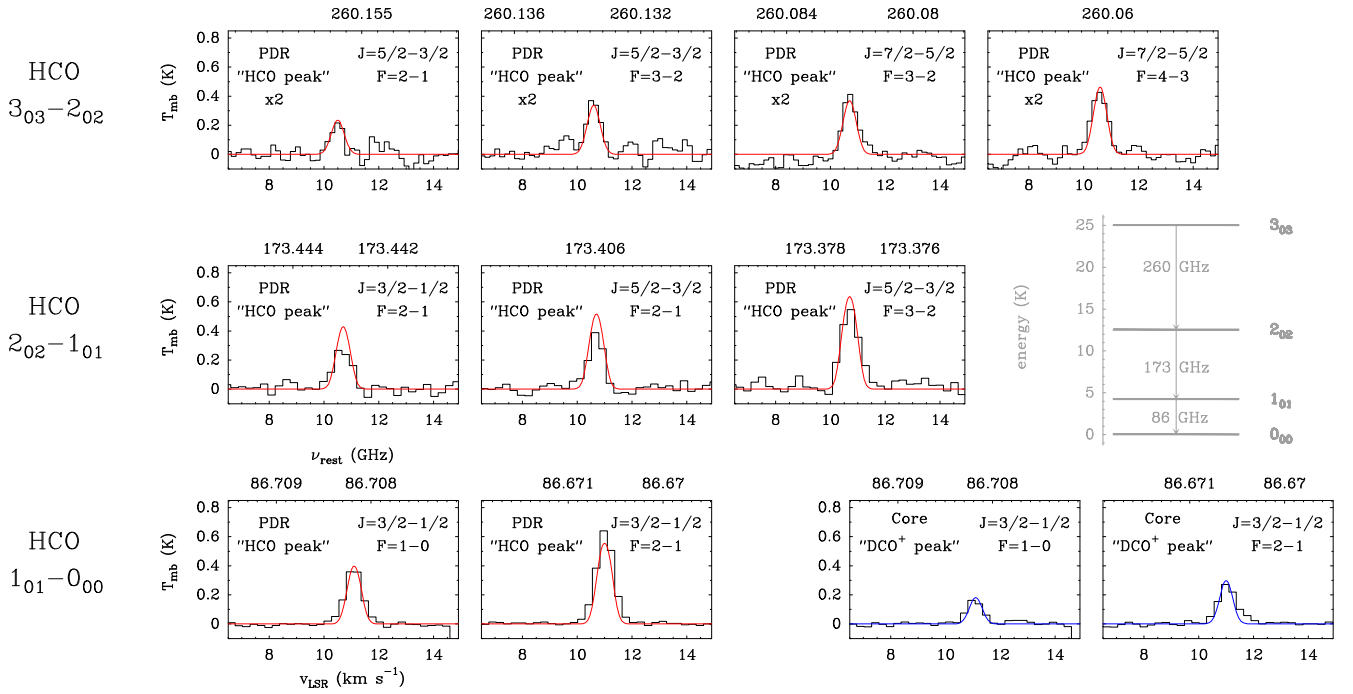


Fig. 2. IRAM-30m observations (histograms) of several HCO hyperfine components of the $1_{01}-0_{00}$, $2_{02}-1_{01}$ and $3_{03}-2_{02}$ rotational transitions towards the PDR (“HCO peak”) and towards the dense core (“DCO⁺ peak”) (Pety et al. 2007a). Solid lines are single- T_{ex} radiative transfer models of the PDR-filament (red curves) and line-of-sight cloud surface (blue curves). A sketch of the HCO rotational energy levels is also shown (right corner).

“HCO peak” in the PDR and the “DCO⁺ peak” in the FUV-shielded core. Both species exhibit strong variations of their column densities and abundances relative to H_2 between the PDR and the shielded region. In the PDR, we found that both the HCO abundance relative to H_2 ($\chi(\text{HCO}) \approx 1-2 \times 10^{-9}$) and the $\text{HCO}/\text{H}^{13}\text{CO}^+$ column density ratio (≈ 50) are high. These figures are higher than all previously published measurements (at lower angular resolution). Besides, **the formyl radical and HCO⁺ reach similar abundances in the PDR.**

The situation is reversed towards the “DCO⁺ peak”, *i.e.* the observed $\text{HCO}/\text{H}^{13}\text{CO}^+$ column density ratio is lower (≈ 1) than towards the “HCO peak”. Nevertheless, while the bulk of the observed H^{13}CO^+ emission arises from cold and shielded gas, the origin of HCO emission is less clear. HCO could either (i) coexist with H^{13}CO^+ or (ii) arise predominantly from the line-of-sight cloud surface. In the former case, our observations show that the HCO abundance drops by one order of magnitude between the PDR and the dense core environment. However, it is possible that the abundance variation is even more pronounced, if the detected HCO emission arises from the line of sight cloud surface. We have estimated the depth of the cloud layer, assuming that HCO keeps the “PDR abundance” in this foreground layer: a cloud surface layer of $A_V \approx 3$ (illuminated by the mean FUV radiation field around the region) also reproduces the observed HCO lines towards the cold dense core (blue solid lines in Fig. 2).

In this case, both the HCO abundance and the $\text{HCO}/\text{H}^{13}\text{CO}^+$ abundance ratio in the dense core itself will be even lower than listed in table 4. We have tried to discriminate both scenarios by comparing the $\text{HCO } 1_{01} - 0_{00}$ ($J=3/2-1/2$, $F=2-1$) and $\text{H}^{13}\text{CO}^+ J=1-0$ line profiles towards this position. Both lines have been observed simultaneously with the IRAM-30m telescope. Because of their very similar frequencies (~ 86.7 GHz), the beam profile and angular resolution is effectively the same.

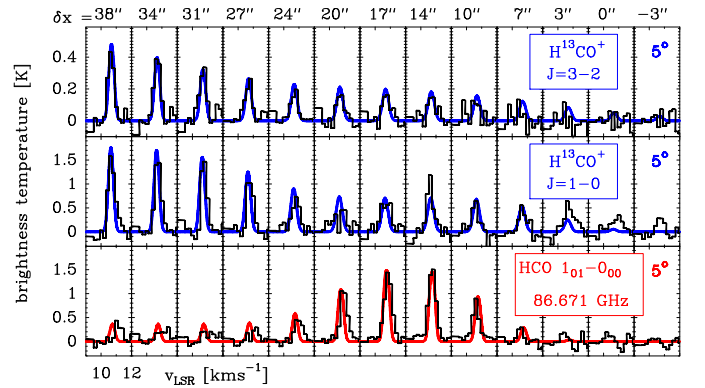


Fig. 3. Observations along a horizontal cut through “the HCO peak” (histograms). The $\text{H}^{13}\text{CO}^+ J=1-0$ and $\text{HCO } 1_{01} - 0_{00}$ lines were mapped with the PdBI at an angular resolution of $6.8''$, whereas the $\text{H}^{13}\text{CO}^+ J=3-2$ line was mapped with HERA-30m (and smoothed to a spatial resolution of $13.5''$). Radiative transfer models of an edge-on cloud with a line of sight extinction of $A_V=20$, inclined 5° relative to the line of sight for HCO (red curve), and H^{13}CO^+ (blue curves) are shown. The single- T_{ex} HCO model assumes a $12''$ width filament with a column density of $3.2 \times 10^{13} \text{ cm}^{-2}$, while $N(\text{HCO})$ is $4.6 \times 10^{12} \text{ cm}^{-2}$ behind the filament. The H^{13}CO^+ model assumes a constant density of $n(\text{H}_2)=5 \times 10^4 \text{ cm}^{-3}$ with $T_k=60 \text{ K}$ and $N(\text{H}^{13}\text{CO}^+)=5.8 \times 10^{11} \text{ cm}^{-2}$ for $\delta x < 35''$; and $T_k=10 \text{ K}$ and $N(\text{H}^{13}\text{CO}^+)=7.6 \times 10^{11} \text{ cm}^{-2}$ for $\delta x > 35''$. Modeled line profiles have been convolved with an appropriate Gaussian beam corresponding to each PdBI synthesized beam or 30m main beam resolution.

In this situation, any difference in the measured linewidths reflects real differences in the gas kinematics and turbulence of

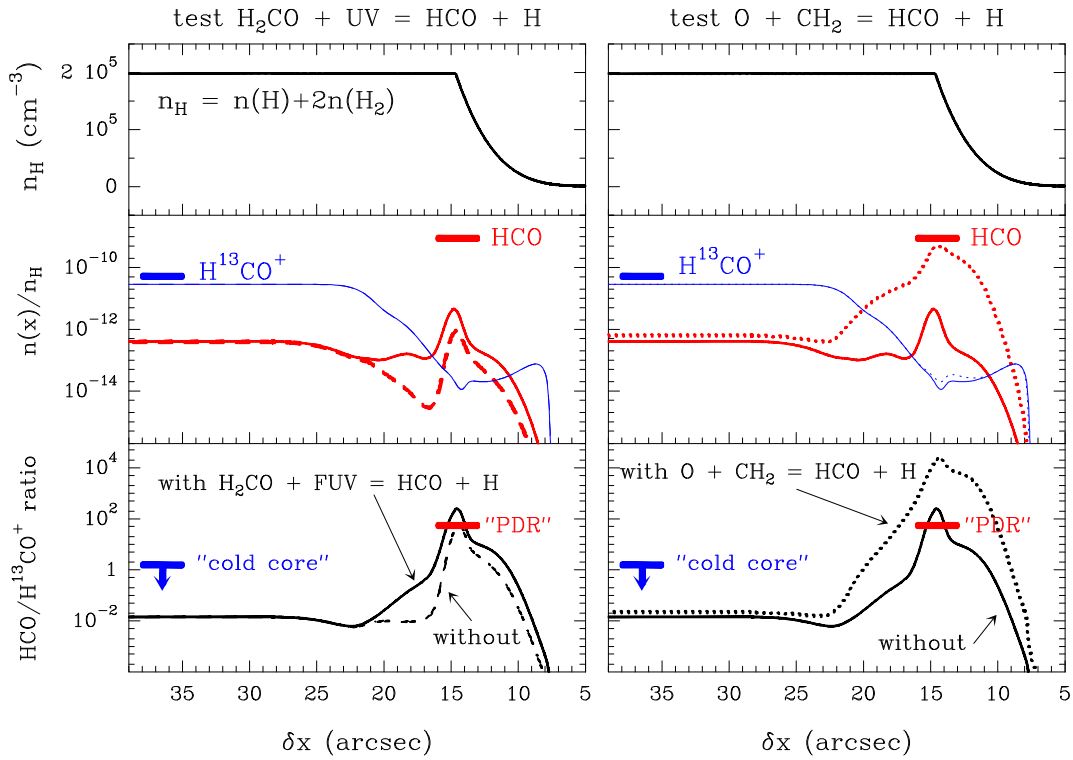


Fig. 4. Photochemical models of a unidimensional PDR. *Upper panels* show the density gradient ($n_H = n(H) + 2n(H_2)$) in cm^{-3} used in the calculation. *Middle panels* show the predicted HCO and H^{13}CO^+ abundances (relative to n_H). The H^{13}CO^+ abundance inferred from observations in the cold core (“the DCO^+ peak”, see the offsets in Table 2) is shown with blue lines. The HCO abundance inferred from observations in the PDR (“the HCO peak”, see the offsets in Table 2) is shown with red lines. *Lower panels* show the $\text{HCO}/\text{H}^{13}\text{CO}^+$ abundance ratio predicted by the models whereas the $\text{HCO}/\text{H}^{13}\text{CO}^+$ column density ratio inferred from observations is shown as blue arrows and red lines (for the cold core and PDR respectively). Every panel compares two different models: **Left-side models** show a *standard chemistry* (dashed curves) versus the same network upgraded with the addition of the $\text{H}_2\text{CO} + \text{photon} \rightarrow \text{HCO} + \text{H}$ photodissociation (solid curves). **Right-side models** show the previous upgraded *standard* model (solid curves) versus a chemistry that adds the $\text{O} + \text{CH}_2 \rightarrow \text{HCO} + \text{H}$ reaction with a rate of $5.01 \times 10^{-11} \text{ cm}^3 \text{ s}^{-1}$ (dotted curves). The inclusion of the $\text{O} + \text{CH}_2$ reaction has almost no effect on H^{13}CO^+ for the physical conditions prevailing in the Horsehead, but triggers an increase of the HCO abundance in the PDR by two orders of magnitude.

the regions where the line profiles are formed. Gaussian fits of the HCO and H^{13}CO^+ lines towards “the DCO^+ peak” provides line widths of $\Delta v(\text{HCO}) = 0.81 \pm 0.06 \text{ km s}^{-1}$ and $\Delta v(\text{H}^{13}\text{CO}^+) = 0.60 \pm 0.01 \text{ km s}^{-1}$. Therefore, even if the H^{13}CO^+ $J=1-0$ line are slightly broadened by opacity and do not represent the true line of sight velocity dispersion, HCO lines are broader at the 3σ level of confidence. This remarkable difference supports scenario (ii) where the H^{13}CO^+ line emission towards the “the DCO^+ peak” arises from the quiescent, cold and dense core, whereas HCO, in the same line of sight, arises predominantly from the warmer and more turbulent outer cloud layers. We note that the presence of a foreground layer of more diffuse material ($A_V \sim 2$ mag) was already introduced by Goicoechea et al. (2006), to fit the CS $J=2-1$ scattered line emission. The analysis of CO $J=4-3$ and $\text{Cl } ^3P_1 - ^3P_0$ maps led also (author?) (Philipp et al. 2006) to propose the presence of a diffuse envelope, with $A_V \sim 2$ mag, and which contributes to roughly the about half the mass of the dense filament traced by C^{18}O and the dust continuum emission. The hypothesis of a surface layer of HCO is therefore consistent with previous modeling of molecular emission of the horsehead.

We conclude 1) that HCO and HCO^+ have similar abundances in the PDR, and 2) that the HCO abundance drops by at least one order of magnitude between the dense and warm PDR region and the cold and shielded DCO^+ core.

4. HCO chemistry

4.1. Gas-phase formation: PDR models

In order to understand the HCO and H^{13}CO^+ abundances and $\text{HCO}/\text{H}^{13}\text{CO}^+$ column density ratio inferred from observations, we have modeled the steady state gas phase chemistry in the Horsehead edge. The density distribution in the PDR is well represented by a density gradient $n_H(\delta x) \propto \delta x^4$, where δx is the distance from the edge towards the cloud interior and $n_H = n(H) + 2n(H_2)$ (see the top panels of Fig. 4). The density reaches a constant n_H value of $2 \times 10^5 \text{ cm}^{-3}$ in an equivalent length of $\sim 10''$ (Habart et al. 2005; Goicoechea et al. 2006). The cloud edge is illuminated by a FUV field 60 times the mean interstellar radiation field ($G_0 = 60$ in Draine units). We used the Meudon PDR code², a photochemical model of a unidimensional PDR (see Le Bourlot et al. 1993; Le Petit et al. 2006; Goicoechea & Le Bourlot 2007, for a detailed description). Our standard chemical network is based on a modified version of *Ohio State University (osu)* gas-phase network, updated for photochemical studies (see Goicoechea et al. 2006). It also includes ^{13}C fractionation reactions (Graedel et al. 1982) and specific computation of the ^{13}CO photodissociation rate as a function of depth. The ionization rate due to cosmic rays in the

² Publicly available at <http://aristote.obspm.fr/MIS/>

models is $\zeta=5\times 10^{-17}\text{ s}^{-1}$. Following our previous works, we chose the following elemental gas phase abundances: $\text{He}/\text{H}=0.1$, $\text{O}/\text{H}=3\times 10^{-4}$, $\text{C}/\text{H}=1.4\times 10^{-4}$, $\text{N}/\text{H}=8\times 10^{-5}$, $\text{S}/\text{H}=3.5\times 10^{-6}$, $^{13}\text{C}/\text{H}=2.3\times 10^{-6}$, $\text{Si}/\text{H}=1.7\times 10^{-8}$ and $\text{Fe}/\text{H}=1.0\times 10^{-9}$.

In Fig. 4, we investigate the main gas-phase formation routes for HCO in a series of models "testing" different pathways leading to the formation of HCO. HCO and H^{13}CO^+ predictions are shown in Figure 4 (middle panels). As a first result, note that in all models the HCO abundance peaks near the cloud surface at $A_V \simeq 1.5$ ($\delta x \simeq 14''$) where the ionization fraction is high ($e^-/\text{H} \simeq 5\times 10^{-5}$). Due to the low abundance of *metals* in the model (as represented by the low abundance of Fe), the ionization fraction in the shielded regions is low ($e^-/\text{H} \lesssim 10^{-8}$), and therefore the H^{13}CO^+ predictions matches the observed values (Goicoechea et al. 2009). Besides, a low metallicity reduces the efficiency of charge exchange reactions of HCO^+ with metals, e.g.,



which are the main gas-phase formation route of HCO in the FUV-shielded gas in our models. Hence, the HCO abundance remains low inside the core. Nevertheless, despite that such models do reproduce the observed HCO distribution, which clearly peaks at the PDR position, the predicted absolute HCO abundances can vary by orders of magnitude depending of the dominant formation route.

In our *standard* model (left-side models : dashed curves), the formation of HCO in the PDR is dominated by the dissociative recombination of H_2CO^+ , while its destruction is dominated by photodissociation. Even if the predicted $\text{HCO}/\text{H}^{13}\text{CO}^+$ abundance ratio satisfactorily reproduces the value inferred from observations, the predicted HCO abundance peak is ~ 3 orders of magnitude lower than observed. In order to increase the gas-phase formation of the HCO in the PDR we have added a new channel in the photodissociation of formaldehyde, the production HCO, in addition to the normal channel producing CO :



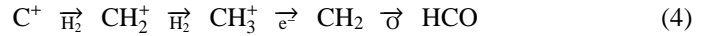
This channel is generally not included in standard chemical networks but very likely exists (Troe 2007; Yin et al. 2007). We included this process with an unattenuated photodissociation rate of $\kappa_{\text{diss}}(\text{H}_2\text{CO})=10^{-9}\text{ s}^{-1}$ and a depth dependence given by $\exp(-1.74A_V)$. This is the same rate as the one given by van Dishoeck (1988) for the photodissociation of H_2CO producing CO, which is explicitly calculated for the Draine (1978) radiation field. Model results are shown in Fig. 4 (left-side models: solid curves). The inclusion of Reaction 2, which becomes the dominant HCO formation route, increases the HCO abundance in the PDR by a factor ~ 5 . But the HCO production rate is still too low to reproduce the abundance determined from observations.

Another plausible possibility to increase the HCO abundance in the PDR by pure gas-phase processes is to include additional reactions of atomic oxygen with carbon radicals that reach high abundances only in the PDR. Among the investigated reactions, the most critical one,



is known to proceed with a relatively fast rate at high temperatures ($5.01\times 10^{-11}\text{ cm}^3\text{ s}^{-1}$ at $T_k=1200\text{--}1800\text{ K}$; Tsuboi & Hashimoto 1981). This is the rate recommended by NIST (Mallard et al. 1994) and UMIST2006 (Woodall et al. 2007) and that we adopt for our lower temperature domain ($\sim 10\text{--}200\text{ K}$).

Model predictions are shown in Fig. 4 (right-side models: dotted curves). Whereas the predicted HCO abundance in the shielded gas remains almost the same, the HCO abundance is dramatically increased in the PDR (by a factor of ~ 125) and the O + CH_2 reaction becomes the HCO dominant production reaction. Therefore, such a pure gas-phase model adding reactions 2 and 3 not only reproduces the H^{13}CO^+ abundance in shielded core, but also reproduces the observed HCO absolute abundances in the PDR. In this picture, the enhanced HCO abundance that we observe in the Horsehead PDR edge would be fully determined by the gas-phase chemical path :



The validity of the rate of Reaction 3 used in our PDR model remains, of course, to be confirmed theoretically or experimentally at the typical ISM temperatures (10 to 200 K).

4.2. Other routes for HCO formation: Grain photodesorption

If Reaction 3 is not included in the chemical network, the predicted HCO abundance is ~ 2 orders of magnitude below the observed value towards the PDR. As a consequence, the presence of HCO in the gas-phase should be linked to grain mantles formation routes, and subsequent desorption processes (not taken into account in our modeling). In particular, Schilke et al. (2001) proposed that HCO could result from H_2CO photodissociation, if large quantities of formaldehyde are formed on grain mantles and then released in the gas phase. Even with this assumption, their model could not reproduce the observed HCO abundance in highly illuminated PDRs such as the Orion Bar. The weaker FUV-radiation field in the Horsehead, but large density, prevent dust grains to acquire high temperatures over large spatial scales. In fact, both gas and grains cool down below $\sim 30\text{ K}$ in $\simeq 10''\text{--}20''$ (or $A_V \simeq 1\text{--}2$) as the FUV-radiation field is attenuated. Therefore, thermal desorption of dust ice-mantles (presumably formed before σ -Orionis ignited and started to illuminate the nebula) should play a negligible role. Hence a non-thermal desorption mechanism should be considered to produce the high abundance of HCO observed in the gas phase. This mechanism could either produce HCO directly or a precursor molecule such as formaldehyde.

Since high HCO abundances are only observed in the PDR, FUV induced ice-mantle photo-desorption (with rates that roughly scales with the FUV-radiation field strength) seems the best candidate (e.g., Willacy & Williams 1993; Bergin et al. 1995). Laboratory experiments have shown that HCO radicals are produced in irradiated, methanol containing, ice mantles (Bernstein et al. 1995; Moore et al. 2001; Bennett & Kaiser 2007). The formyl radical could be formed through the hydrogenation of CO in the solid phase. It is an important intermediate radical in the synthesis of more complex organic molecules such as methyl formate or glycolaldehyde (Bennett & Kaiser 2007). However, the efficiency of the production of radicals in FUV irradiated ices remains uncertain, and very likely depends on the ice-mantle composition. The formation of species like formaldehyde and methanol in CO-ice exposed to H-atom bombardment has been reported by different groups (Hiraoka et al. 1994; Watanabe et al. 2002; Linnartz et al. 2007), further confirming the importance of HCO as an intermediate product in the synthesis of organic molecules in ices. Indeed, hydrogenation reactions of CO-ice, which form HCO, H_2CO , CH_3O and CH_3OH in grain mantles (e.g., Tielens & Whittet 1997; Charnley et al. 1997), are one important path which warrants further studies.

To compare with our observations, we further need to understand how the radicals are released in the gas phase, either directly during the photo-processing, or following FUV induced photo-desorption. Recent laboratory measurements have started to shed light on the efficiency of photo-desorption, which depends on the ice composition and molecule to be desorbed. For species such as CO, the rate of photo-desorbed molecules per FUV photon is much larger than previously thought (e.g., Öberg et al. 2007). Similar experiments are required to constrain the formation rate of the various species that can form in interstellar ices and to determine their photo-desorption rates.

We can use the measured gas phase abundance of HCO to constrain the efficiency of photo-desorption. We assume that the PDR is at steady state, and that the main HCO formation mechanism is non thermal photo-desorption from grain mantles (with a F_{HCO} rate), while the main destruction mechanism is gas-phase photodissociation (with a D_{HCO} rate), therefore :

$$D_{HCO} = G_0 \kappa_{\text{diss}}(\text{HCO}) \chi(\text{HCO}) n(\text{H}_2) \quad [\text{cm}^{-3} \text{s}^{-1}] \quad (5)$$

$$F_{HCO} = G_0 \kappa_{\text{pd}}(\text{HCO}) \chi(\text{HCO}_{\text{ice}}) \frac{n(\text{H}_2\text{O}_{\text{ice}})}{n(\text{H}_2)} n(\text{H}_2) [\text{cm}^{-3} \text{s}^{-1}] \quad (6)$$

where $\chi(\text{HCO})$ is the gas phase abundance of HCO relative to H_2 , $\chi(\text{HCO}_{\text{ice}})$ is the solid phase abundance relative to water ice, and $n(\text{H}_2\text{O}_{\text{ice}})/n(\text{H}_2)$ is the fraction of water in the solid phase relative to the total gas density. $\kappa_{\text{diss}}(\text{HCO})$ and $\kappa_{\text{pd}}(\text{HCO})$ are the HCO photodissociation and photo-desorption rates respectively.

By equating the formation and destruction rates, we get :

$$\kappa_{\text{pd}}(\text{HCO}) = \kappa_{\text{diss}}(\text{HCO}) \frac{\chi(\text{HCO})}{\chi(\text{HCO}_{\text{ice}})} \frac{n(\text{H}_2)}{n(\text{H}_2\text{O}_{\text{ice}})} \quad [\text{s}^{-1}] \quad (7)$$

or

$$\frac{\kappa_{\text{pd}}(\text{HCO})}{\text{s}^{-1}} \approx 10^{-12} \frac{\kappa_{\text{diss}}(\text{HCO})}{10^{-9}} \frac{\chi(\text{HCO})/10^{-9}}{\chi(\text{HCO}_{\text{ice}})/10^{-2}} \frac{10^{-4}n(\text{H}_2)}{n(\text{H}_2\text{O}_{\text{ice}})} \quad (8)$$

where we have used typical figures for the HCO abundance in the gas phase ($\sim 10^{-9}$, see above) and solid phase ($\sim 10^{-2}$ see e.g. Bennet & Kaiser 2007) and for the amount of oxygen present as water ice in grain mantles.

Assuming standard ISM grains with a radius of $0.1 \mu\text{m}$ the required photodesorption efficiency (or yield) $Y_{\text{pd}}(\text{HCO})$:

$$Y_{\text{pd}}(\text{HCO}) \approx \frac{\kappa_{\text{pd}}(\text{HCO})}{G_0 \exp(-2A_V) \pi a^2} \quad [\text{molecules photon}^{-1}] \quad (9)$$

(see e.g., d'Hendecourt et al. 1985; Bergin et al. 1995) converts to $Y_{\text{pd}}(\text{HCO}) \approx 10^{-4}$ molecules per photon (for the FUV radiation field in the Horsehead and $A_V \approx 1.5$, where HCO peaks). Therefore, the production of HCO in the gas phase from photo-desorption of formyl radicals could be a valid alternative to gas phase production, if the photo-desorption efficiency is high and HCO abundant in the ice mantles. This mechanism also requires further laboratory and theoretical studies.

Because the formyl radical is closely related to formaldehyde and methanol and the three species are likely to coexist in the ice mantles, a combined analysis of the H_2CO , CH_3OH and HCO line emissions towards the Horsehead nebula (PDR and cores) is needed to provide more information on the relative efficiencies of gas-phase and solid-phase routes in the formation of complex organic molecules in environments dominated by FUV-radiation. This will be the subject of a future paper.

5. Summary and conclusions

We have presented interferometric and single-dish data showing the spatial distribution of the formyl radical rotational lines in the Horsehead PDR and associated dense core. The HCO emission delineates the illuminated edge of the nebula and coincides with the PAH and hydrocarbon emission. HCO and HCO^+ reach similar abundances ($\approx 1-2 \times 10^{-9}$) in these PDR regions where the chemistry is dominated by the presence of FUV photons. For the physical conditions prevailing in the Horsehead edge, pure gas-phase chemistry is able to reproduce the observed HCO abundances (high in the PDR, low in the shielded core) if the $\text{O} + \text{CH}_2 \rightarrow \text{HCO} + \text{H}$ reaction is included in the models. This reaction connects the high abundance of HCO, through its formation from carbon radicals, with the availability of C^+ in the PDR.

The different linewidths of HCO and H^{13}CO^+ in the line of sight towards the ‘‘DCO⁺ peak’’ suggest that the H^{13}CO^+ line emission arises from the quiescent, cold and dense gas completely shielded from the FUV radiation, whereas HCO predominantly arises from the outer surface of the cloud (its illuminated *skin*). As a result we propose the $\text{HCO}/\text{H}^{13}\text{CO}^+$ abundance ratio, and the HCO abundance itself (if $\gtrsim 10^{-10}$), as sensitive diagnostics of the presence of FUV radiation fields. In particular, regions where the $\text{HCO}/\text{H}^{13}\text{CO}^+$ abundance ratio (or intensity ratio if lines are optically thin) is greater than ≈ 1 should reflect ongoing FUV-photochemistry.

Given the rich HCO spectrum and the possibility to map its bright millimeter line emission with interferometers, we propose $\text{HCO}-\text{H}_2$ as a very interesting molecular system for calculations of the *ab initio* inelastic collisional rates.

Acknowledgements. We thank the IRAM PdBI and 30m staff for their support during the observations. We thank A. Faure and J. Tennyson for sending us the $\text{H}^{13}\text{CO}^+-e^-$ collisional rates prior to publication, B. Godard for useful discussions on the chemistry of carbon ions in the diffuse ISM, and A. Bergeat and A. Canosa for interesting discussions on radical-atom chemical reactions. JRG is supported by a *Ramón y Cajal* research contract from the Spanish MICINN and co-financed by the European Social Fund. This research has benefited from the financial support of the CNRS/INSU research programme, PCMI. We acknowledge the use of the JPL (Pickett et al. 1998) and Cologne (Müller et al. 2001; Müller et al. 2005) spectroscopic data bases, as well as the UMIST chemical reaction data base (Woodall et al. 2007).

References

- Abergel A., Bernard J. P., Boulanger F., et al., 2002, A&A, 389, 239
- Bennett, C.J., and Kaiser, R.I., 2007, ApJ 661, 899
- Bergin, E.A., Langer, W.D. & Goldsmith, P.F. 1995, ApJ, 441, 222.
- Bernstein M.P., Sandford, S.A., Allamandola, L.J., Chang S., and Scharberg M. A., 1995, ApJ 454, 327
- Charnley, S.B., Tielens, A.G.G.M. & Rodgers, S.D. 1997, ApJ, 482, L203
- d’Hendecourt, L. B., Allamandola, L. J. & Greenberg, J. M. 1985, A&A, 152 130
- Draine, B. T. 1978, ApJS, 36, 595.
- de Jong, T., Boland, W., Dalgarno, A. 1980, A&A, 91, 68
- Flower, D.R., 1999, MNRAS, 305, 651
- García-Burillo, S., Martín-Pintado, J., Fuente, A., Usero, A. & Neri, R. 2002, ApJ, 575, L55
- Goicoechea, J. R., Pety, J., Gerin, M., Teyssier, D., Roueff, E., Hily-Blant, P. & Baek, S. 2006, A&A, 456, 565.
- Goicoechea, J. R. & Le Bourlot, J. 2007, A&A, 467, 1.
- González-García, M, Le Bourlot, J., Le Petit, F. & Roueff, E. 2008, A&A, 485, 127.
- Graedel, T. E., Langer, W. D., & Frerking, M. A. 1982, ApJS, 48, 321.
- Habart, E., Abergel, A., Walmsley, C. M., Teyssier, D. & Pety, J. 2005, A&A, 437, 177-188.
- Hiraoka, K., Ohashi, N., Kihara, N., Yamamoto, K., Sato, T. & Yamashita, A. 1994, Chem. Phys. Lett., 229, 408
- Landsberg, B. M., Merer, A. J., & Oka, T. 1977, J.Mol.Spec, 67, 459

- Le Bourlot, J., Pineau Des Forets, G., Roueff, E., & Flower, D. R. 1993, A&A, 267, 233
- Le Petit, F., Nehmé, C, Le Bourlot, J. & Roueff, E. 2006, ApJS, 64, 506
- Linnartz, H., Acharyya, K., Awad, Z. et al. 2007, *Molecules in Space and Laboratory*, J.L. Lemaire & F. Combes (eds)
- Mallard et al., 1994, NIST Chemical Kinetics Database, NIST, Gaithersburg, MD.
- Müller H.S.P., Thorwirth S., Roth D.A., and Winnewisser W., A&A 370, L49.
- Müller H.S.P., Schlöder F., Stutzki J., and Winnewisser W., J. Mol. Struct. 742, 215.
- Öberg, K.I., Fuchs, G.W., Awad, Z., Fraser, H.J., Schlemmer, S., van Dishoeck, E.F., Linnartz, H., 2007, ApJ, 662, L23.
- Moore M.H., Hudson R.L., Gerakines P.A., 2001, Spec. Acta part A, 57, 843.
- Penzias, A.A. & Burrus, C.A. 1973, ARA&A, 11, 51.
- Pety, J., Teyssier, D., Fossé, D., Gerin, M., Roueff, E., Abergel, A., Habart, E. & Cernicharo, J. 2005, A&A, 435, 885-899
- Pety, J. SF2A-2005: Semaine de l'Astrophysique Française, meeting held in Strasbourg, France, 2005, Edited by F. Casoli, T. Contini, J.M. Hameury and L. Pagani. Published by EdP-Sciences, Conference Series, 2005, p. 721.
- Pety, J., Goicoechea, J. R., Hily-Blant, P., Gerin, M. Teyssier, D. 2007, A&A, 464, L41
- Pety J., Goicoechea, J. R., Gerin, M., et al., 2007, Proceedings of the *Molecules in Space and Laboratory* conference, J.L. Lemaire & F. Combes (eds).
- Philipp S. D., Lis D. C., G'usten R., Kasemann C., Klein T., Phillips T. G., 2006, A&A 454, 213
- Pickett H.M., Poynter R.L., Cohen E.A., et al., J. Quant. Spectrosc. & Rad. Transfer 60, 883.
- Röllig, M. et al. 2007, A&A, 467, 187.
- Schilke, P., Pineau des Forets, G., Walmsley, C. M. & Martín-Pintado, J. 2001, A&A, 372, 291
- Snyder, L. E., Hollis, J. M. & Ulich, B. L. 1976, ApJ, 208, L91
- Snyder, L. E., Schenewerk, M. S. & Hollis, J. M. 1985, ApJ, 298, 360
- Tielens, A.G.G.M. & Whittet, D.C.B. 1997, in *Molecules in astrophysics: probe and processes*, ed. E.F. van Dishoeck (Dordrecht, Kluwer), 45
- Troe, J. 2007, J. Phys. Chem., 111, 3868
- Teyssier, D., Fossé, D., Gerin, M., Pety, J., Abergel, A. & Roueff, E. 2004, A&A, 417, 135.
- Tsuboi, T. & Hashimoto, K. 1981, J. Combust. Flame, 42
- van Dishoeck, E. F. 1988, Rate Coefficients in Astrochemistry. Editors, T.J. Millar, D.A. Williams; Publisher, Kluwer Academic Publishers, Dordrecht, Boston, 49.
- Watanabe, N. & Kouchi, A. 2002, ApJ, 571, L173,
- Willacy, K., & Williams, D.A. 1993, MNRAS, 260, 635.
- Woodall, J., Agúndez, M., Markwick-Kemper, A. J. & Millar, T. J. 2007, A&A, 466, 1197
- Yin, H.M., Rowling, S.T., Büll, A. & Kable, S.H. 2007, J. Chem. Phys., 064302

Online Material

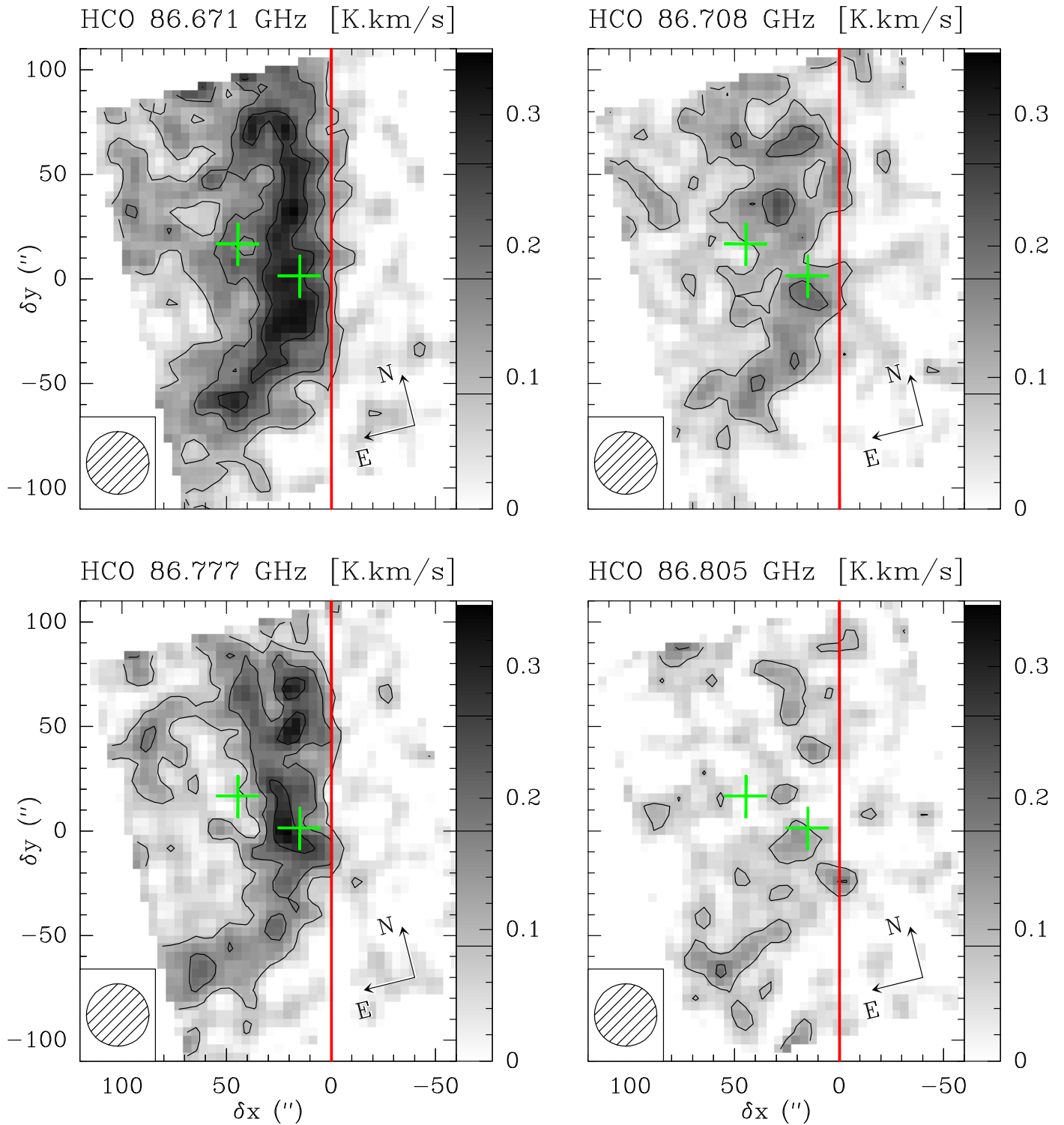


Fig. 5. Medium angular resolution maps of the integrated intensity of the 4 hyperfine components of the fundamental transition of HCO. These lines have been observed simultaneously at IRAM-30m. Maps have been rotated by 14° counter-clockwise around the projection center, located at $(\delta x, \delta y) = (20'', 0'')$, to bring the illuminated star direction in the horizontal direction and the horizontal zero has been set at the PDR edge. The emission of all lines is integrated between 9.6 and 11.4 km s⁻¹. Displayed integrated intensities are expressed in the main beam temperature scale. Contour levels are displayed on the grey scale lookup tables. The red vertical line shows the PDR edge and the green crosses show the positions (DCO⁺ and HCO peaks) where deep integrations have been performed at IRAM-30m (see Fig. 2).